



Article

Development of a Novel Lightweight Utility Pole Using a New Hybrid Reinforced Composite—Part 2: Numerical Simulation and Design Procedure

Qianjiang Wu and Farid Taheri *

Department of Mechanical Engineering, Dalhousie University, Halifax, NS B3H 4R2, Canada;
qianjiang.wu@dal.ca

* Correspondence: farid.taheri@dal.ca

Abstract: The first paper of this two-part series discussed the development of a novel lightweight 3D wood dowel-reinforced glass epoxy hybrid composite material (3DdrFRP) and its manufacturing procedures. It also experimentally compared the performance of scaled utility poles made from conventional 2D E-glass epoxy and 3DdrFRP materials. In the second part, the development of robust, efficient, and fairly accurate nonlinear finite element (FE) models is outlined. The models are calibrated based on experimental results and used to simulate the performance of equivalent 2D and 3D poles, proving the integrity of the numerical models. Additionally, a simplified analytical calculation method is developed for practicing engineers to evaluate the stiffness of 3D-DrFRP poles fairly accurately and quickly.

Keywords: 3D hybrid composites; composite poles; numerical simulation; progressive composite material model; finite element method; LS-DYNA



Citation: Wu, Q.; Taheri, F. Development of a Novel Lightweight Utility Pole Using a New Hybrid Reinforced Composite—Part 2: Numerical Simulation and Design Procedure. *J. Compos. Sci.* **2024**, *8*, 50. <https://doi.org/10.3390/jcs8020050>

Academic Editor: Francesco Tornabene

Received: 28 November 2023

Revised: 16 January 2024

Accepted: 22 January 2024

Published: 30 January 2024



Copyright: © 2024 by the authors. Licensee MDPI, Basel, Switzerland. This article is an open access article distributed under the terms and conditions of the Creative Commons Attribution (CC BY) license (<https://creativecommons.org/licenses/by/4.0/>).

1. Introduction

In the initial section of these papers, a detailed history of utility poles was presented, highlighting the advantages of fiber-reinforced polymer composite (FRP) poles [1]. Notably, companies such as RS Technologies Inc. design modular GFRP poles, providing transportation efficiency and facilitating the easy replacement of failed modules [2].

Moving to the second part, the finite element method is utilized to design two poles: a modular 2D cross-ply E-glass epoxy pole and a prismatic pole made of the wood dowel-reinforced 3D E-glass epoxy hybrid composite. This study underscores the significance of FEM in achieving cost-effective and durable laminated composite poles.

While there is currently no established unified design methodology for FRP poles, the CSA Group suggests using load factors akin to those applied for steel poles [3]. Our study incorporates FEM to design the aforementioned poles, emphasizing critical performance, and loading conditions [4], and considering factors such as cost and durability with minimal testing requirements. Notably, this design approach aligns with modern aircraft structural design practices involving laminated composites, as observed in aircraft like the Boeing 787 and the Airbus A350 XWB [5,6].

2. Numerical Simulation Framework

As discussed in the first part of this series [7], and as shown in Figure 1, 3DdrFML is a complex hybrid material, consisting of a 4 mm thick 3D E-glass fabric epoxy with wooden dowels inserted into its channels. The fabric is made of two layers of cross-ply fabrics separated by a series of glass threads, hereafter referred to as pillars. The dowels were 3.175 mm diameter Ramin hardwood dowels. The dowels were purchased from a local hardware store; therefore, no specific information was available for them. The dowels were not pretreated by any chemical or coating. It is important to note that the diameter

of the dowels used was slightly larger than the width and height of the fabric channels of the untreated fabric. Therefore, the dowels had to be carefully inserted into every other channel along the warp direction. West System 105 room-cured resin and 206 hardener (WEST SYSTEM, 2014, Bay City, MI, USA) were used to prepare the 3D FRP. The resin and hardener were mixed thoroughly with a ratio of 5:1, and the mixture was then brushed onto the wood-core-inserted fabric as per the 3D fabric vendor’s instruction (note that the detail of the peel ply and other hand-layup fabrication materials are not noted for brevity’s sake). Different element types, constituent materials, and contact algorithms were used to develop a modelling framework for simulating 3DdrFML’s performance.

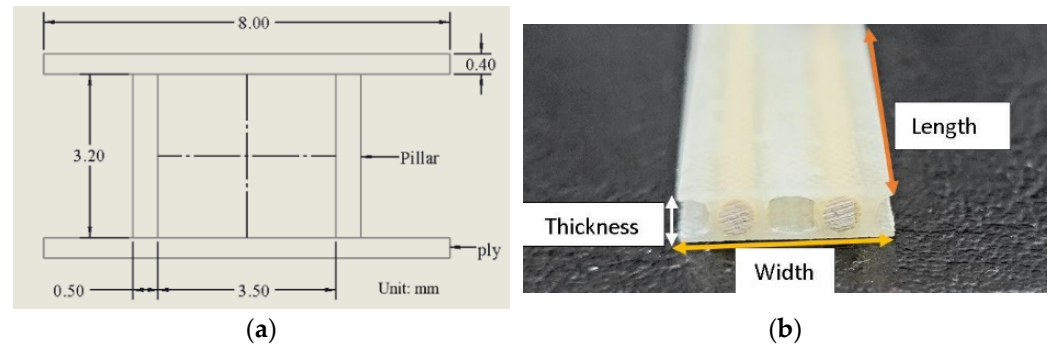


Figure 1. (a) The dimensions of the 3D E-glass epoxy unit cell used in all numerical models; (b) a view of the actual flexural specimen.

2.1. Simulation of the Behaviour of the Flexural 3DdrFML Specimens

In this study, the behaviour of the 3DdrFML test specimens considered in the first part of the paper was simulated, focusing on various computational algorithms. To assess these, a preliminary finite element model mimicking a flexural test was created, with dimensions of 153 (L) × 15 (W) × 4 (T) mm (Figure 1). Due to symmetry, only a quarter model was needed (see Figure 2).

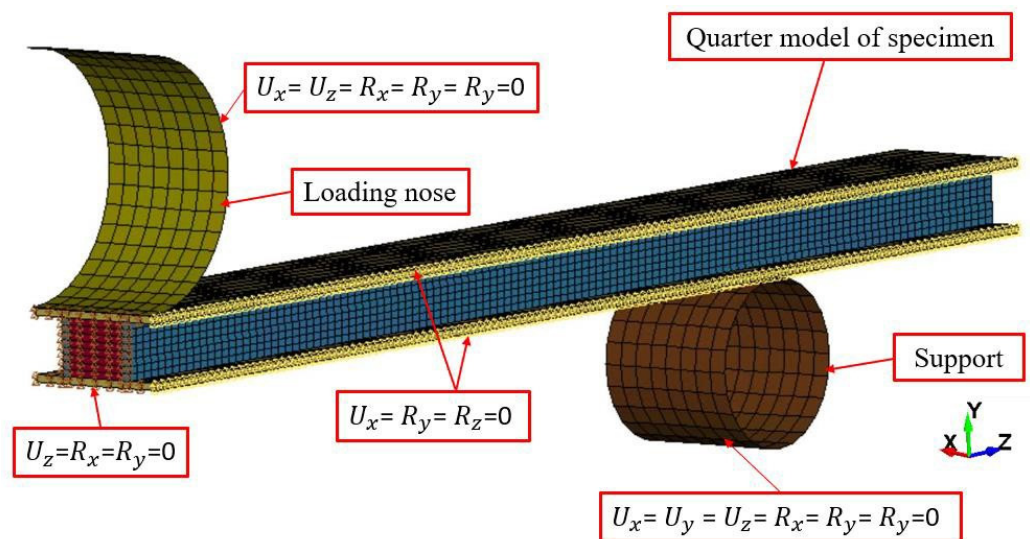


Figure 2. The quarter symmetry model of the flexural test specimens and the imposed boundary conditions.

The selective reduced-integrated (SRI) Tshell element [8] was incorporated for modelling plies and pillars to prevent shear-locking. The dowels were modelled using solid elements with the SRI formulation, which accounted for poor aspect ratios. The resin contact interfaces between the dowels and surrounding fabrics and pillars were modelled using the

automatic surface-to-surface tie-break contact algorithm, with the option of incorporating the cohesive zone model (CZM) to account for potential delamination or loss of contact between dowels and FRP. A bilinear CZM model was incorporated with its parameters evaluated in our earlier investigation [9] as presented in Table 1.

Table 1. Summary of the epoxy-related parameters required by the CZM contact algorithm.

| Normal Failure Stress (MPa) | Shear Failure Stress (MPa) | Mode I Energy Release Rate (KJ/m ²) | Mode II Energy Release Rate (KJ/m ²) | Penalty Stiffness (N/mm ³) |
|-----------------------------|----------------------------|---|--|--|
| 59 | 23 | 1.5 | 2 | 3500 |

The model also considered loading nose-to-specimens and supports' nose-to-specimen interfaces using the "automatic surface-to-surface" contact algorithm, with frictional coefficients set to 0.3. Additionally, the "eroding surface-to-surface algorithm" was incorporated to address potential fabric layer ruptures.

The constitutive composite material model (MAT_054) was used for describing 3D fabric epoxy and its pillars, which includes an enhanced damage detection algorithm [10]. The material model incorporated into the analysis is an arbitrary orthotropic material designed to work in conjunction with the Chang–Chang failure criterion. It is important to mention that the erosion of elements in MAT_54 is not controlled solely based on the failure criterion. Instead, element erosion is initiated by five critical strain values, which are associated with four strain-to-failure values measurable through coupon-level tests in the positive fiber direction (tension) DFAILT, in the negative fiber direction (compression) DFAILC, in the matrix direction DFAILM, and in-plane shear DFAILS. The existence of these triggers indicates the use of the Hashin failure criterion rather than the Chang–Chang criterion.

To further clarify:

When the DFAILT parameter (or other parameters) is set to zero, an element is considered failed upon meeting the tension failure mode based on the Chang–Chang stress-based criteria.

If DFAILT is assigned a non-zero value, element failure is determined by the strain surpassing the defined limit, including DFAILT, DFAILC, DFAILM, and DFAILS, in any direction, triggering the Hashin criteria.

If the effective failure strain (EFS) is set to a positive value, element failure occurs when the effective strain within the element exceeds the designated EFS computed using ultimate normal and shearing strains.

When the criterion for element deletion based on timestep size (TFAIL) is set to a positive value ($0 < \text{TFAIL} \leq 0.1$), an element is considered failed when its timestep becomes smaller than TFAIL. Conversely, if TFAIL is greater than 0.1, the element is deleted when the ratio of the current timestep to the original timestep falls below TFAIL.

As can be appreciated, the input of accurate material failure strains is critical when modelling FRP materials with this material model. It should also be noted that when the second criterion is met, the first criterion (Chang–Chang criterion) continues to influence the element's strength. In such scenarios, the Chang–Chang criterion parameters establish the element's maximum strengths. In other words, the element will not be eroded (deleted) when the criterion is met; instead, the stress value will maintain the element at that prescribed maximum strength until the element erodes according to the defined failure strains. For a deeper understanding of specific terminology, the user is directed to LS-DYNA's theory manual [8].

The mechanical properties used are shown in Table 2. The dowel's properties were based on published results [11] and tuned using experimental data, using LS-DYNA's MAT_143 orthotropic material for wood [12]. The pillar fibers were oriented at 30° with respect to the through-thickness axis of the fabric. The refined material properties used in flexural and compressive models are listed in Table 2.

Table 2. Refined material properties used in flexural and compressive models.

| | | | | | | | |
|-----------------------|--------------------------------|-------------------|-------------------|-------------------|-------------------|-------------------|-------------------|
| Upper and lower plies | ρ (g/mm ³) | E_{11} (MPa) | E_{22} (MPa) | ν_{21} | G_{12} (MPa) | G_{23} (MPa) | G_{31} (MPa) |
| | X_c (MPa) | X_T (MPa) | Y_c (MPa) | Y_T (MPa) | S_{12} (MPa) | ϵ_{T1} | ϵ_{C1} |
| Pillars | ρ (g/mm ³) | E_{11} (MPa) | E_{22} (MPa) | ν_{21} | G_{12} (MPa) | G_{23} (MPa) | G_{31} (MPa) |
| | X_c (MPa) | X_T (MPa) | Y_c (MPa) | Y_T (MPa) | S_{12} (MPa) | ϵ_{T1} | ϵ_{C1} |
| Dowels | ρ (g/mm ³) | E_L (MPa) | E_T (MPa) | G_{LT} (MPa) | G_{LR} (MPa) | ν_{21} | X_c (MPa) |
| | X_c (MPa) | Y_c (MPa) | Y_c (MPa) | S_{12} (MPa) | | | |

2.2. Results and Discussions

Figure 3 illustrates a comparison of load–displacement responses. Table 3 presents the results of the numerical simulation of a typical flexural specimen, with its results closely matching the experimental results. When considering the responses of all specimens for result averaging, an error margin of 10.5% is observed. However, as seen, the response of specimen 4 significantly deviates from that of the other specimens, possibly due to the complex nature of the hybrid composite and fabrication-related issue(s) that may be manifested significantly in small-sized specimens. Therefore, if one considers this response as an outlier, the average error is reduced significantly to 3.2%. Therefore, the numerical results are deemed acceptable, demonstrating the accuracy of the developed numerical framework.

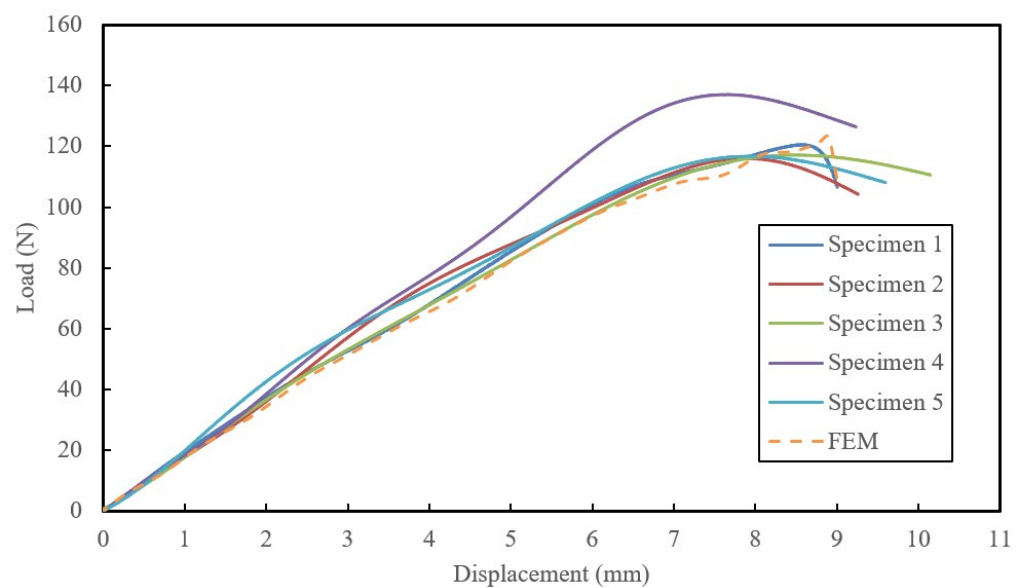


Figure 3. Comparison of the load–displacement responses of the flexural specimens and the numerically predicted results.

To further validate the model, the damage patterns predicted by the numerical model were compared to the actual specimen response. The FE model successfully simulated

ply and pillar failures by deleting highly stressed elements in the damaged region. As shown in Figure 4, depicting the midspan failure of a typical specimen, the most vulnerable region was the ply region on top of the empty channel, a scenario accurately captured by the numerical simulation. The simulated response of compression test specimens, with summarized results in Table 4 and a comparison of experimental and numerical failure modes corresponding to a location above the mid-height of the specimen, is also illustrated in Figure 5. As can be observed, the shear crimping of the wood dowel and delamination and local buckling of the 3D fabric have also been successfully captured by the numerical model. In the images produced by the numerical analysis, the colours red, blue and brown signify the cross-ply layers and pillars of the 3D fabric, and wood dowels, respectively.

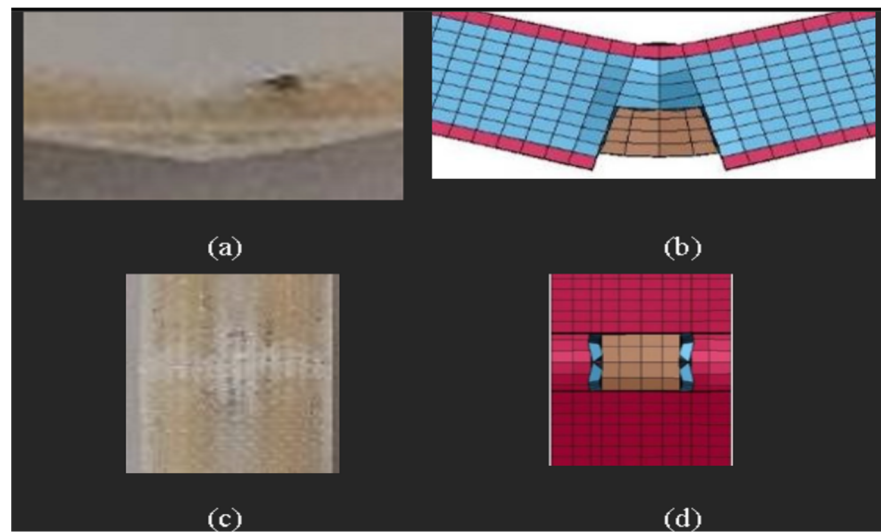


Figure 4. Comparison of the post-failure damage on the actual specimen and the numerically predicted; (a,b) show the side view and (c,d) show the top view.

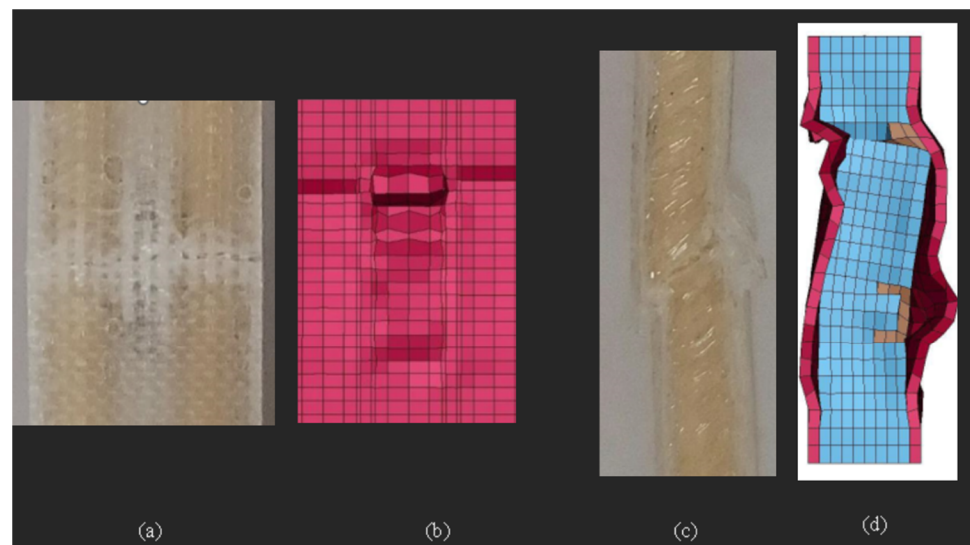


Figure 5. Compression of the experimental and numerically predicted compressive failure modes of a 3DdrFRP specimen under compressive loading: (a) experimental front view, (b) numerical front view, (c) experimental side view; (d) numerical side view.

Table 3. Comparison of the average experimental values against the numerically predicted.

| | Max Load (N) | Max. Disp. (mm) | E_f (MPa) | Flexural Rigidity (N·mm ²) | % Error |
|-----|--------------|-----------------|-------------|--|---------|
| Exp | 134.0 | 8.6 | 10,267.1 | 679,683.3 | 10.5 |
| FEM | 128.0 | 8.9 | 9188.42 | 608,273.1 | |

Table 4. Comparison of the average experimental values and the numerically predicted values.

| | Elastic Modulus, E_C (MPa) | Ultimate Load (N) | Ultimate Strength (MPa) | Ultimate Strain (mm/mm) | % Error in Elastic Modulus |
|-----|------------------------------|-------------------|-------------------------|-------------------------|----------------------------|
| Exp | 8963.5 | 2747.0 | 69.5 | 0.015 | 9.9 |
| FEM | 8080.0 | 2556.0 | 61.4 | 0.017 | |

3. Pole Designs

With confidence in the established mechanical properties and numerical algorithms, the design and analysis of two types of scaled-down composite poles, (i) a conventional 2D FRP (like commercially available poles) and (ii) the introduced 3D-drFRP material, were carried out. While the 2D pole was designed in a modular form due to its advantages, the 3D poles could not take advantage of modularity. Both pole types were designed using 3D solid layered elements for material failure examination, utilizing the Maximum Stress failure criterion for optimal laminate stacking sequence.

3.1. Preliminary Analyzes

3.1.1. Establishment of an Effective Layup

In spite of the availability of advanced failure criteria for assessing in-plane failure in LS-DYNA, evaluating interlaminar failure necessitates the use of the 3D solid layered element. However, this limits the examination to material failures based solely on the Maximum Stress Failure criterion. Consequently, before finalizing the design of both 2D and 3D poles, a preliminary analysis was conducted to ascertain effective ply sequencing and optimal element types.

To investigate the optimal stacking sequence for a laminate with constant thickness, a comprehensive model was constructed in LS-DYNA utilizing its 3D solid elements. Various layups, comprising unidirectional (UD) E-glass fibers and biaxial [0/90] glass fabrics (also known as cross-ply layup), were scrutinized for potential initiation of interlaminar failure. The model, representing a 2 m long prismatic pole, incorporated dimensions and boundary conditions as outlined in Table 5.

Table 5. Particulars of the test pole to examine the effect of various ply sequences.

| Geometric Features | Length = 2000 mm | ID = 48 mm | Total Thickness = 2.6 |
|---------------------|-----------------------------------|---|---------------------------|
| Boundary conditions | Pole embedment height (mm) 200 | Distance of load from the tip (mm) 100 | Load magnitude (N) 793 |

The analysis results are reported in Table 6. In the table, the passing criterion is denoted by “P,” while a failed criterion is identified by “F”. Note that these properties enable an examination of through-thickness stresses; the MAT_059, known as the “SOLID COMPOSITE FAILURE SOLID MODEL” in LS-DYNA, was employed. This material model encompasses eight failure modes as described earlier, including normal tension and compression failures in orthogonal directions, as well as in-plane and out-of-plane shears.

The analysis results revealed that the [+ / 0₉ / +] laminate, chosen for its practicality and adequate stiffness, emerged as a suitable layup for fabrication, surpassing the [013] layup, which exhibited the highest stiffness. Additionally, the [90 / 0₁₁ / 90] stacking sequence was also explored to assess interlaminar stresses. These findings contribute valuable insights for optimizing design decisions in the pursuit of enhanced structural performance.

Table 6. Numerical failure indices for various laminated designs.

| | [+2/0 ₅ /+2] | [+4/0 ₅] | [90/0 ¹¹ /90] | [+7] | [013] | [+/0 ₉ /+] | [+/90/0 ₉ /90/+] |
|---------------------------------------|-------------------------|----------------------|--------------------------|------|-------|-----------------------|-----------------------------|
| Longitudinal tension failure | F | F | P | F | P | P | F |
| Transverse tension failure | P | P | F | P | P | P | F |
| In-plane shear failure | F | F | P | F | P | P | F |
| Through-thickness tension failure | F | F | F | F | P | P | F |
| Through-thickness shear failure | P | P | P | P | P | P | F |
| Longitudinal compression failure | F | F | P | F | P | P | F |
| Transverse compression failure | P | P | P | P | P | P | P |
| Through-thickness compression failure | F | P | F | P | P | P | F |

NOTE: F stands for “failed”, P stands for “passed” and ‘+’ signifies cross-ply fabric (e.g., +₄ ply sequence represents four layers of cross-ply fabrics).

3.1.2. Influence of Element Formulation

The influence of element formulation was explored by comparing the performance of 3D solid elements to Tshell elements. Tshell is an effective eight-node shell element with a 2D stress state similar to a thin shell. A Penalty function is used to constrain the top and bottom cross-ply layers’ nodes; in other words, the thickness can only change by a membrane strain (similar to the thin shell). This element produces fairly accurate results compared to the 3D solid element with significant efficiency.

The tip displacement of the pole with [+ / 0₉ / +] layup was analyzed using both element types. The results reported in Table 7 showed that the Tshell element provided good accuracy with significantly lower CPU consumption, improving efficiency by 3856%. Both elements provided sufficiently accurate results, with small margins of error compared to the analytical solution. As seen, while the model constructed with solid elements produced error margins of approximately 1/3 of the error margins produced by the model constructed of Tshell elements, the significant saving in the CPU warrants the use of TShell elements in this analysis.

Table 7. Comparison of the theoretical maximum tip deflection and bending stress of the pole against numerically predicted values based on the element type.

| | Solid Elements | Tshell Elements | Analytical | Solid Elements % Error | Tshell Elements % Error |
|------------------------------|----------------|-----------------|------------|------------------------|-------------------------|
| Maximum deflection (mm) | 349.3 | 361.8 | 352 | 0.7 | 2.8 |
| Maximum bending stress (MPa) | 133 | 116 | 137.3 | 3.2 | 15.5 |
| CPU Time (s) | 989 | 25 | - | - | - |

3.2. Design of the Modular Pole Made of 2D Fabric

The design of the 2D modular pole involved two one-meter-long modules due to limitations in the hand layup fabrication process. The pole was designed with a [+ / 0₉ / +] layup with the specific dimensions of its module reported in Table 8 and tested against a commercially available pole [2] and other designs from the literature (see Table 9). The modelling considered symmetry, and the Tshell element was used for half of the pole. The overlap region dimensions were designed according to ASCE’s recommendations [4]. To conserve CPU, nodes within the overlap region were merged with the boundary condition and applied to all the inner surface nodes within a 235 mm distance measured from the bottom edge of fully constrained (identified with red triangular symbols in Figure 6a). The damage model (MAT_054) was implemented, with mechanical properties provided by Ekşi and Genel [13], as tabulated in Table 10.

Table 8. The proposed modular pole design’s dimensions.

| Module | Length (mm) | Upper Dia. (mm) | Lower Dia. (mm) | Thickness (mm) | Taper Angle (Deg.) | Overlap Length |
|--------|-------------|-----------------|-----------------|----------------|--------------------|----------------|
| Upper | 1000 | 47.2 | 54.2 | 2.6 | 0.2 | 135.2 |
| Lower | 880 | 48.1 | | | | |

Table 9. Comparison of the proposed pole design with the commercial pole and scaled poles from other studies.

| | Proposed Design (Assembled) | RS Technologies | Pole of Ref. [14] | Pole of Ref. [15] |
|-------------------|-----------------------------|-----------------|-------------------|-------------------|
| Slenderness ratio | 165.7 | 219.2 | 127.7 | 83.0 |
| D_{avg}/t | 20.7 | 27.5 | 19.4 | 65.5 |

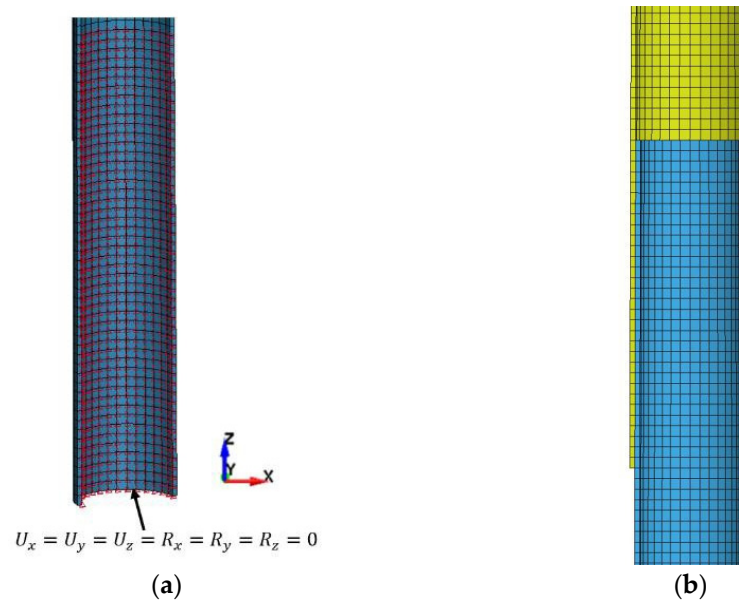


Figure 6. (a) Illustration of boundary conditions accounting for the fixture; (b) mesh of the overlap region of the tapered poles.

Table 10. Mechanical properties used in the FE model of the 2D modular pole.

| Fabric Type | ρ (g/mm ³) | E_{11} (MPa) | E_{22} (MPa) | ν_{21} | G_{12} (MPa) | G_{23} (MPa) | G_{31} (MPa) |
|-------------|--------------------------------|-------------------|-------------------|----------------|-------------------|-------------------|-------------------|
| UD | 0.00175 | 15,560 | 6749 | 0.11 | 3310.8 | 2595.8 | 3310.8 |
| | X_c (MPa) | X_T (MPa) | Y_c (MPa) | Y_T (MPa) | S_{12} (MPa) | | |
| | 343.3 | 572.2 | 80.1 | 78 | 30.9 | | |
| Biaxial [+] | ρ (g/mm ³) | E_{11} (MPa) | E_{22} (MPa) | ν_{21} | G_{12} (MPa) | G_{23} (MPa) | G_{31} (MPa) |
| | 0.00175 | 9336 | 4049.4 | 0.11 | 1986.4 | 1557.5 | 1655.4 |
| | X_c (MPa) | X_T (MPa) | Y_c (MPa) | Y_T (MPa) | S_{12} (MPa) | | |
| | 223.1 | 343.3 | 48.1 | 46.8 | 18.5 | | |

The comparison of the numerical simulation and experimental load–deflection results illustrated in Figure 7 shows good agreement, with the numerical results being slightly stiffer due to the inherent nature of FEM. Figure 8 exhibits the comparison of strain variations in the poles. The maximum numerical strain reached -0.018 mm/mm at approximately 540 mm deflection, compared to the experimental strain of -0.015 mm/mm at the same deflection. The tensile experimental strain–deflection curves were consistent, and the numerically predicted strains were slightly higher up to a tip deflection of 190 mm

when inelastic deformation occurred. The maximum compressive and tensile strains were comparable for both experimental and numerical values.

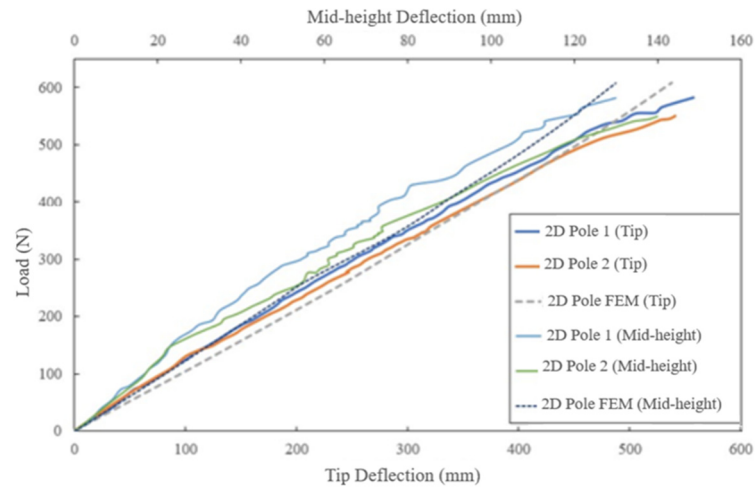
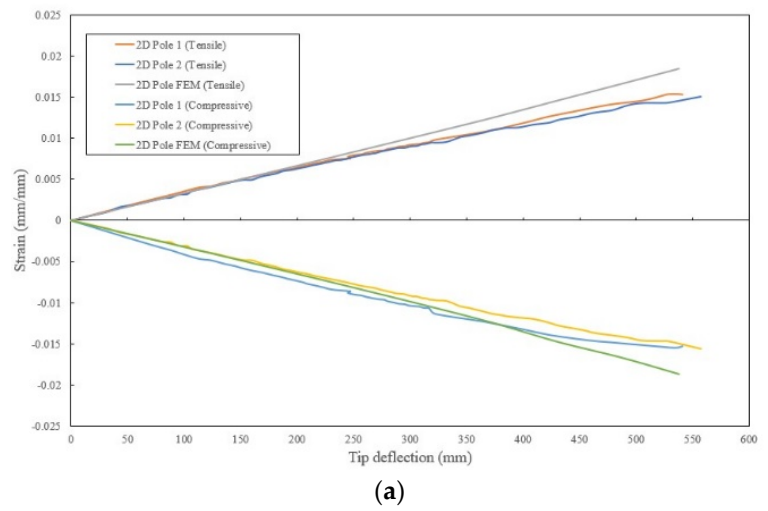
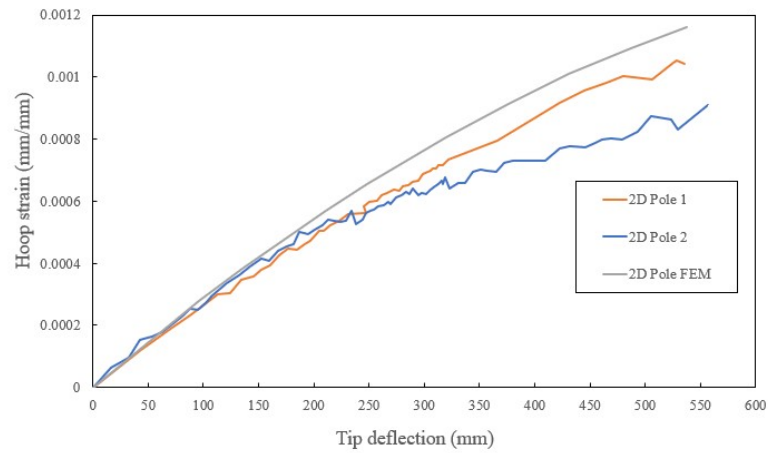


Figure 7. Comparison of the experimental and numerical load–deflection curves of the 2D poles at the tip and mid-height.



(a)



(b)

Figure 8. Comparison of the variation in the experimental and numerically obtained results: (a) tensile and compressive strains; (b) hoop strain, as a function of the applied tip displacement.

3.3. Scaled Pole Design

As stated previously, one of the novel aspects of this work is the incorporation of 3D fabric in developing long-lasting poles, which has not been attempted before. Another novelty is the addition of wooden dowels to reinforce the fabric, enhancing its stiffness and enabling the use of 3D fabric in cylindrical structural members. Before designing the 3D pole, three-point bending tests were conducted on curved specimens extracted from a 3DdrFRP cylinder. The results in Figure 7 from the previous paper show that dowel reinforcement improved the FRP’s stiffness and strength by approximately 300% and 500%, respectively.

Due to the complex configuration of 3DdrFRP, fabricating a tapered pole would be challenging. The tapered shape would result in a differing number of channels on the top and bottom portions, requiring partial cutting of the dowels along the pole’s length. This impracticality led to the use of a prismatic pole design as a compromise. The pole had specific dimensions with a slenderness ratio close to that of 2D tapered poles, as discussed in the first paper. The pole’s restraint and loading conditions are depicted in Figure 9.

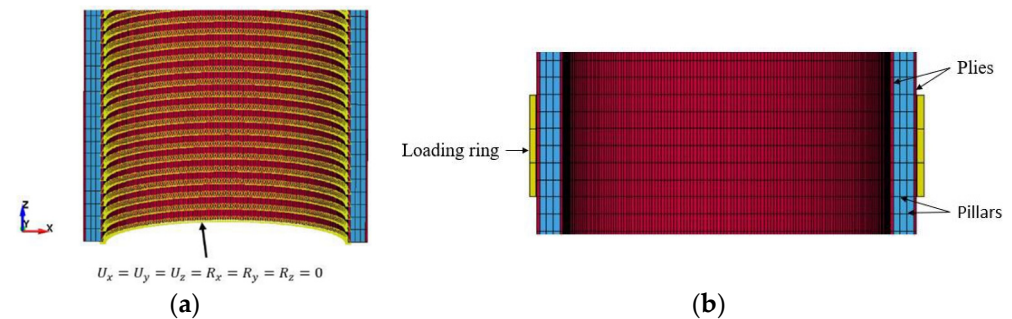


Figure 9. (a) The fully restrained nodes on the inner surface of the pole; (b) the load ring attached to the pole using the contact algorithm.

The designed pole was subjected to the same load as the 3D poles in the experimental investigation. A comparison of the experimental and numerical load–tip deflection curves is shown in Figure 10. The predicted response closely matched the experimental results up to the poles’ failure loads. The FE model’s prediction estimated the pole’s failure load at a slightly lower deflection and a failure load magnitude between the two experimental poles.

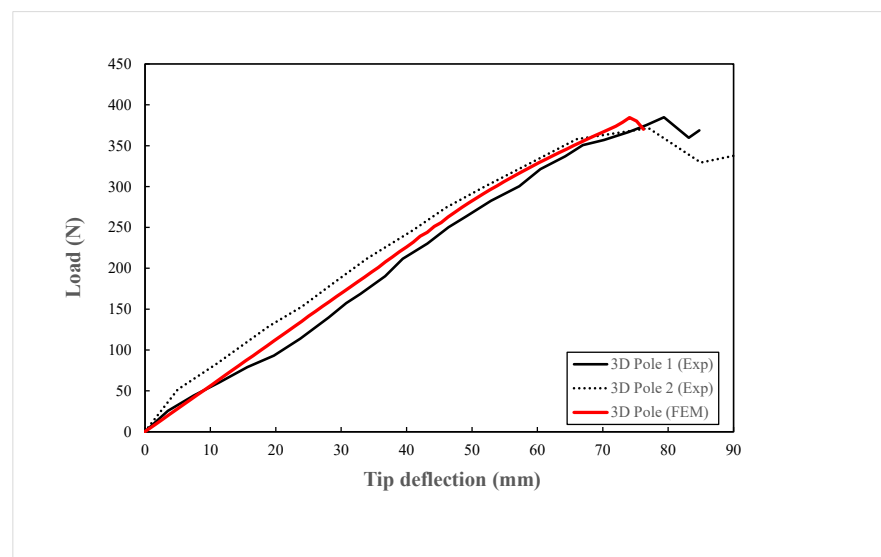


Figure 10. Comparison of the experimental and numerically predicted load–deflection curves.

Figure 10 shows that pole 2 endured a significant load after reaching its ultimate strength, then gradually decreasing to 262 N before fully fracturing at 220 mm deflection. This was accompanied by ply failure above the groundline along an empty channel on the compression side, followed by compression failure observed at the groundline after the fracture. Figure 11 illustrates the comparison of numerically predicted tensile strain values with experimental results, showing close agreement. The ultimate experimental and FE strains and their corresponding deflections are nearly identical to those observed on the compression side of the poles. Similar modes of failure as described in Section 2.2 were also captured in these models. In other words, slight local buckling on the compressively stressed part of the pole near the groundline could be observed (see Figure 12), with some regions of the cross-ply failing and eroding. In the figure, elements in yellow represent the inner and outer crossply layers of the 3D fabric, blue represents the pillars and elements in green represent the wood dowels.

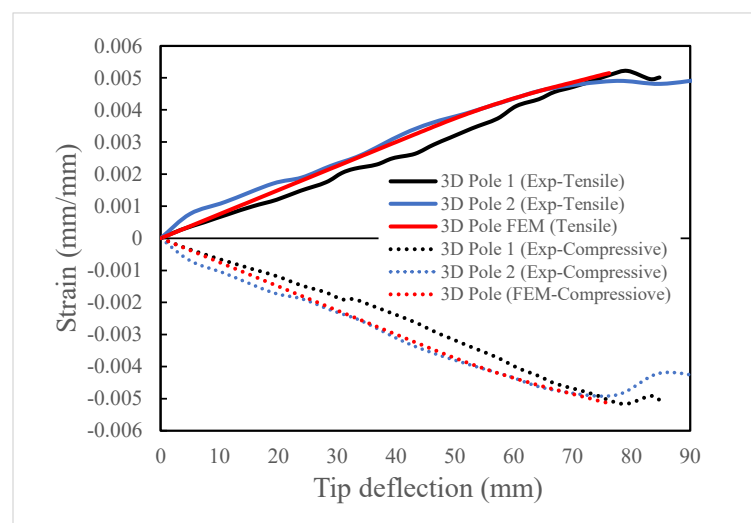


Figure 11. Comparison of experimental and FE strain–tip deflection curves for 3D poles.

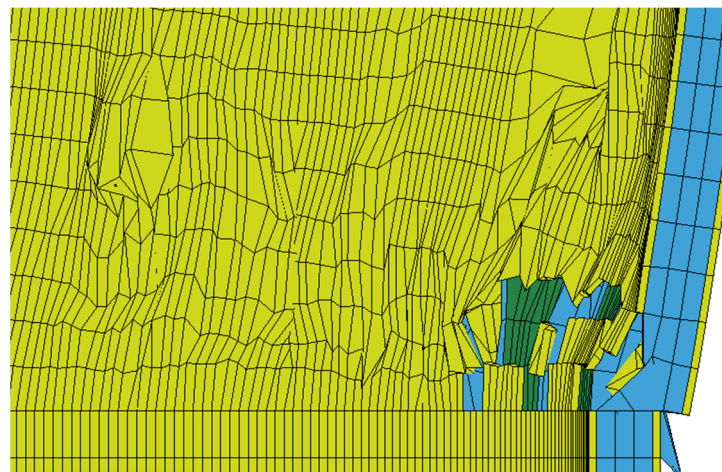


Figure 12. Local buckling model of the pole near the groundline on the compressive side of the pole. Note: Colors yellow, blue and green signify the cross-ply layers and pillars of the 3D fabric, and wood dowels, respectively.

The average experimental and numerically predicted stiffness values are obtained based on the load-to-tip deflection and reported in Table 11. The percentage error of the numerically predicted stiffness is only 0.89%, which is very low, thus validating the numerical model's integrity.

Table 11. Comparison of the averaged elastic modulus of the actual and numerically designed poles.

| | Moment of inertia, I (mm^4) | E_x (MPa) | Stiffness ($\text{N}\cdot\text{mm}^2$) | % Error in E_x |
|------------|--|-------------|--|------------------|
| Experiment | | 9726.5 | 1.12×10^9 | |
| FEM | 115,149.5 | 9639.6 | 1.11×10^9 | 0.89 |

4. Comparison of the Performance of 2D and 3D Poles

The performances of the two types of poles are compared by normalizing their ultimate strength to their masses. Since the tested 3D poles were shorter and prismatic, and the 2D poles were longer and non-prismatic, they could not be compared directly. Therefore, the response of a 3D pole with the same length as the 2D pole is simulated. The outside diameter of this 3D pole is the average of the outside top and bottom diameters of the 2D pole. Additionally, for more consistency, an equivalent prismatic 2D pole is also considered to investigate the effect of the modular design of the 2D pole in comparison to the monolithic pole. The length and outside diameter of these prismatic 2D and 3D poles are the same as the average length and diameter of the modular 2D poles (i.e., 1735 mm and 48 mm, respectively). The results of the analyses are reported in Table 12 and shown in Figure 13.

Table 12. Summary of the fundamental physical parameters of the FE model and the results.

| Pole Type | Volume (mm^3) | Mass (g) | Stiffness ($\text{N}\cdot\text{mm}^2$) | Ultimate Load Capacity (N) | Normalized Ultimate Load Capacity (N/kg) |
|------------------------|--------------------------|----------|--|----------------------------|--|
| 2D Pole | 68,6711 | 760.5 | 1.02×10^9 | 616.0 | 0.81 |
| 2D Prismatic Pole | 57,2920 | 634.5 | 9.02×10^8 | 530.0 | 0.84 |
| Long Prismatic 3D Pole | 66,9842 | 729.2 | 1.06×10^9 | 355.8 | 0.49 |

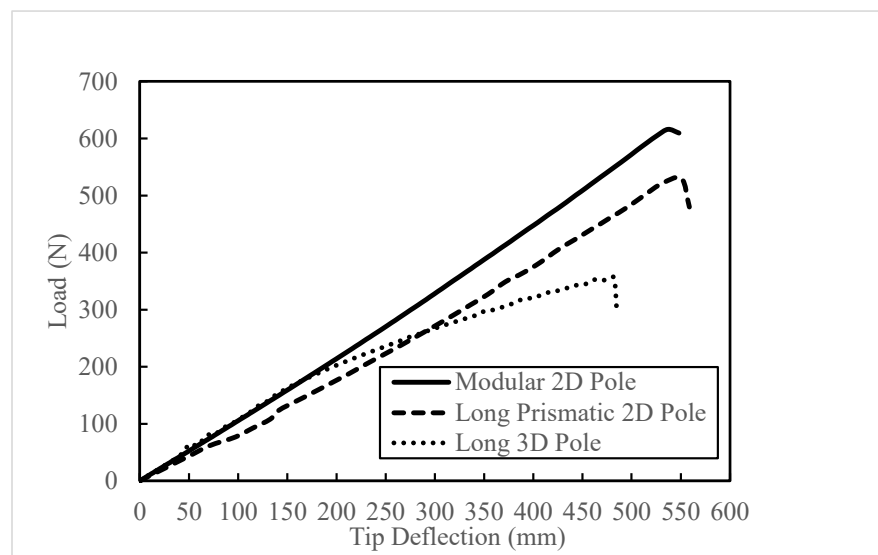


Figure 13. Comparison of the 2D and 3D poles.

As seen, the modular 2D and the longer 3D poles exhibit similar initial stiffness, while the prismatic 2D pole’s stiffness is slightly lower. Surprisingly, the 3D pole’s ultimate strength is noticeably lower than both 2D poles. The 3D pole starts to show damage at a load of 195 N, with a tip deflection of 190 mm, whereas the 2D poles show no damage until reaching their ultimate strength. It should be noted that the 2D poles consist of more fabric layers than the 3D poles.

The unsupported segments of the 3D pole, specifically those over the empty channels, make it more prone to premature failure under a flexure load compared to the segments

supported by wood dowels and pillars. The addition of more layers of 2D-FRP or dowel reinforcement in every channel of the 3D fabric could significantly improve its performance.

5. A Simple Equation for Establishing the Stiffness of 3D Poles

With the consideration of Figure 1a, a simple equation for estimating the stiffness of 3D poles is developed below, by which the extensional elastic modulus of the complex hybrid composite in the principal material direction is established.

$$E_{3D,x} \approx E_{3D,1}(\text{exact}) = \frac{2A_{\text{Ply}} E_{\text{Ply}} + 2A_{\text{Pillar}} E_{\text{Pillar}} + A_{\text{Dowel}} E_{\text{Dowel}}}{2A_{\text{Ply}} + 2A_{\text{Pillar}} + A_{\text{Dowel}}} \quad (1)$$

where A_{Ply} , A_{Pillar} and A_{Dowel} are the total cross-sectional areas of the ply, pillar, dowel and empty channels, respectively; E_{Ply} , E_{Pillar} and E_{Dowel} are the elastic modulus of the plies, pillars and dowels in the principal material direction 1, respectively.

This equation can be modified and used with the exact net cross-section area or the gross cross-section area, simplifying the calculation process, as follows:

$$E_{3D,x} \approx E_{3D,1}(\text{approx}) = \frac{2A_{\text{Ply}}E_{\text{Ply}} + 2A_{\text{Pillar}} E_{\text{Pillar}} + A_{\text{Dowel}} E_{\text{Dowel}} + A_{\text{air}} E_{\text{air}}}{2A_{\text{Ply}} + 2A_{\text{Pillar}} + A_{\text{Dowel}} + A_{\text{air}}} \quad (2)$$

where E_{air} is the elastic modulus of the air in the empty channels (equal to zero) and A_{air} is the total cross-section area of the empty channels. Multiplication of this value of $E_{3D,x}$ with the gross cross-section area would yield exactly the same extensional stiffness as obtained by the use of the exact net cross-section area. The results from the equations are reported in Table 13.

Table 13. Comparison of experimental Young’s modulus and those predicted by the established equations.

| Method | Extensional Elastic Modulus (MPa) | Stiffness (N·mm ²) | % Error in Stiffness |
|---------------------------------------|-----------------------------------|--------------------------------|----------------------|
| Experimental value (Compression Test) | 8963.5 | 152,208 | |
| Equation (1) | 8686.0 | 152,154 | 0.03 |
| Equation (2) | 5296.0 | 152,154 | |

Equation (2) can be further simplified for the 4 mm nominal thick 3D fabric used in this study, considering that the parameters related to the 3DFRP are constant, and the only variable would be the dowel’s elastic modulus as an unknown. Therefore, the following simplified equation could be used instead of the more elaborate version, Equation (1).

$$E_{3D,x} = 3562.2 + 0.45E_{\text{dowel}} \quad (3)$$

It is important to note that this equation is specific to the configuration considered in this study and can be adapted for different fabric thicknesses or pole cross-sections.

6. Summary and Conclusions

The authors previously introduced a novel, lightweight, and stiff utility pole constructed from an innovative 3D fiberglass fabric epoxy composite material (3DdrFRP) reinforced with wooden dowels. This paper delves into the intricate numerical modelling techniques developed for optimizing the design of these advanced 3D hybrid composite poles. The resulting nonlinear models exhibited a high degree of reliability and accuracy in predicting pole responses, including localized failure modes.

Additionally, this research involved a comparison between LS-DYNA’s 3D solid layered element and its 2D thick-shell (Tshell) counterpart to evaluate prediction accuracy and computational resource utilization. The findings indicated that the Tshell yielded results with acceptable accuracy while drastically improving CPU efficiency, reducing consumption by 3856%.

The numerical analysis further revealed a substantial enhancement in composite stiffness and strength (approximately 300% and 500%, respectively) with the incorporation of dowels into the 3D-FRP composite. The ongoing use of the developed numerical model aims to conduct a parametric study, seeking to optimize the performance of 3D poles and address localized fabric failures effectively.

Author Contributions: Q.W.: conducted the experiments and FE analysis, processed the data and produced most of the drawings. F.T.: secured funding for the project, designed the entire project and managed it; checked all data and results; wrote, edited and proofread the manuscript. All authors have read and agreed to the published version of the manuscript.

Funding: Funding was provided to the second author by the Natural Sciences and Engineering Research Council of Canada (grant No. RGPIN-2017-05114), which is gratefully appreciated and acknowledged.

Data Availability Statement: Some of the data in this research are not publicly available due to restrictions.

Conflicts of Interest: The authors declare no conflict of interest.

References

1. Morrell, J.J. *Wood Pole Maintenance Manual*; Forest Research Laboratory, Oregon State University: Corvallis, OR, USA, 2012.
2. RS Technologies Inc. RS Poles 2023. Available online: <https://www.rs poles.com/> (accessed on 27 November 2023).
3. CSA Group. Overhead Systems. C22.3 No. 1-15 2015. Available online: <https://www.scc.ca/en/standardsdb/standards/27989> (accessed on 27 November 2023).
4. *Recommended Practice for Fiber-Reinforced Polymer Products for Overhead Utility Line Structures*, 2nd ed.; Fecht, G. (Ed.) American Society of Civil Engineers (ASCE): Reston, VA, USA, 2019.
5. Nath, A.; Anand, R.; Desai, J.; Sultan, M.T.H.; Raj, S.A. *Modelling and Finite Element Analysis of an Aircraft Wing Using Composite Laminates*; IOP Conf. Series: Materials Science and Engineering; IOP Publishing: Bristol, UK, 2021. [CrossRef]
6. Siefert, A.; Henkel, F.-O. Nonlinear analysis of commercial aircraft impact on a reactor building—Comparison between integral and decoupled crash simulation. In Proceedings of the Transactions, SMiRT 21, New Delhi, India, 6–11 November 2011.
7. Wu, J.; Taheri, F. Development of a Novel Lightweight Utility Pole using a New Hybrid Reinforced Composite—Part 1: Fabrication & Experimental Investigation. *J. Compos. Sci.* 2023; *in press*.
8. *LS-DYNA Keyword User's Manual*, 13th ed.; Livermore Software Technology: Livermore, CA, USA, 2021; Volume I. Available online: https://ftp.lstc.com/anonymous/outgoing/jday/manuals/ls-dyna_971_manual_k_rev1.pdf (accessed on 27 November 2023).
9. Mohamed, M.; Taheri, F. Influence of graphene nanoplatelets (GNPs) on mode I fracture toughness of an epoxy adhesive under thermal fatigue. *J. Adhes. Sci. Technol.* 2017, 31, 19–20. [CrossRef]
10. *LS-DYNA Keyword User's Manual*, 13th ed.; Livermore Software Technology: Livermore, CA, USA, 2021; Volume II. Available online: https://ftp.lstc.com/anonymous/outgoing/jday/manuals/LS-DYNA_Manual_Volume_II_R9.0.pdf (accessed on 27 November 2023).
11. Wang, K.; Taheri, F. Compressive Residual Strengths of GLARE and a 3DFML. *Polymers* 2023, 15, 1723. [CrossRef]
12. Ross, R. *Wood Handbook: Wood as an Engineering Material*; Forest Service U.S. Department of Agriculture: Washington, DC, USA, 2021.
13. Ekşi, S.; Genel, K. Comparison of Mechanical Properties of Unidirectional and Woven Carbon, Glass and Aramid Fiber Reinforced Epoxy Composites. *Acta Phys. Pol. A* 2017, 132, 879–882. [CrossRef]
14. Altanopoulos, T.I.; Raftoyiannis, I.G.; Polyzois, D. Finite element method for the static behavior of tapered poles made of glass fiber reinforced polymer. *Mech. Adv. Mater. Struct.* 2021, 28, 2141–2150. [CrossRef]
15. Ibrahim, S.M. Performance Evaluation of Fiber-Reinforced Polymer Poles For Transmission Lines. Ph.D. Thesis, Manitoba University, Winnipeg, MB, Canada, 2000.

Disclaimer/Publisher's Note: The statements, opinions and data contained in all publications are solely those of the individual author(s) and contributor(s) and not of MDPI and/or the editor(s). MDPI and/or the editor(s) disclaim responsibility for any injury to people or property resulting from any ideas, methods, instructions or products referred to in the content.